ACS APPLIED MATERIALS & INTERFACES

Research Article

www.acsami.org

Single-Pot Synthesis of ⟨001⟩-Faceted N-Doped Nb_2O_5/Reduced Graphene Oxide Nanocomposite for Efficient Photoelectrochemical Water Splitting

M. Qamar,*[,†] M. Abdalwadoud,[‡] M. I. Ahmed,[†] A.-M. Azad,[†] B. Merzougui,[§] S. Bukola,[†] Z. H. Yamani,[†] and M. N. Siddiqui[‡]

[†]Center of Excellence in Nanotechnology (CENT), King Fahd University of Petroleum and Minerals, Dhahran 31261, Kingdom of Saudi Arabia

[‡]Department of Chemistry, King Fahd University of Petroleum and Minerals, Dhahran 31261, Kingdom of Saudi Arabia

[§]Qatar Environment & Energy Research Institute, Qatar Foundation, Doha 5825, Qatar

Supporting Information

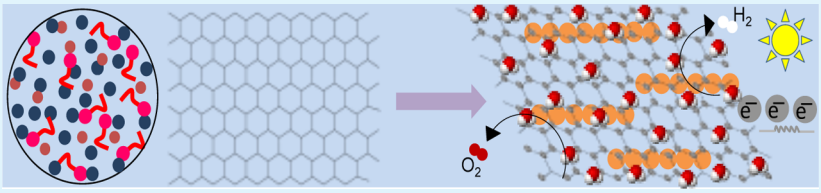

ABSTRACT: Due to exciting catalytic activity and selectivity, tailoring of nanocatalysts consisting of preferred crystal facets and desired structural properties remains at the forefront of materials engineering. A facile one-step nonhydrolytic solvothermal synthesis of a nanocomposite of reduced graphene oxide and one-dimensional nitrogen-doped Nb_2O_5 (N-NbO*x*) with exposed ⟨001⟩ facet is described. Triethylamine performed the dual role as nitrogen source and capping agent to control the size and unidirectional growth of Nb_2O_5 nanocrystallites. The nanocomposite showed efficient visible-light-mediated (λ > 420 nm) water splitting in a photoelectrochemical cell. A plausible mechanism for the formation of N-NbO*x* nanorods and improved photoelectrochemical efficacy in terms of their oriented growth is proposed.

KEYWORDS: *solvothermal, nonaqueous synthesis, semiconductor photocatalyst, water splitting, sunlight*

1. INTRODUCTION

Due to unique physicochemical properties, nanostructured semiconductor photocatalysts are the subject of exhaustive investigation for a number of photocatalytic applications such as water splitting,[1,2] water decontamination,[3,4] CO_2 reduction,[5,6] and so forth. Since semiconductor-mediated photocatalysis is a surface phenomenon, the latter plays a crucial role in the process. It has been well established that the photocatalytic activity is an artifact of the light absorption capabilities, redox rate, and the availability of exciton (electron−hole pairs) on the surface, among others.[7−11] One popular approach to endow surfaces with enhanced catalytic activity is to increase the number of active sites, which is achieved by controlling various parameters such as size, composition, interfacing, porosity, shape, and so forth. Interestingly, shape-tailoring at the nanoscale further is an evolving concept to induce improvement in the catalytic activity and selectivity in nanostructured materials.[12−15] The shape-controlled nanocrystals possess well-defined geometry and morphology, both of which cooperatively enhance their functionality, selectivity, and chemical reactivity. For instance, TiO_2 nanocrystals with high fraction of ⟨101⟩ facets show enhanced photocatalytic hydrogen generation from methanol.[16] On the other hand, Yang et al. found that truncated octahedral TiO_2 with ⟨001⟩ facets were more reactive than the ⟨101⟩ facets for the dissociative adsorption of reactants.[14] Similarly, the ⟨100⟩ CeO_2 nanocubes exhibited superior catalytic activity for CO than the truncated octahedral nanocrystals of CeO_2 enclosed by six ⟨100⟩ and eight ⟨111⟩ facets.[17]

Nb_2O_5 is an n-type semiconductor used extensively in acid catalysis, gas sensing, energy storage, and other applications.[18−20] Recently, the activity of Nb_2O_5 was shown to be closely associated with its shape and surface structure.[21−25] In particular, nanorods of Nb_2O_5 were prepared and shown to possess superior properties in various applications including as humidity sensors,[21] powerful catalysts for vanadium redox flow batteries,[22] high performance dye-sensitized solar cells,[23] biosensors,[24] and so forth. However, Nb_2O_5 nanocrystals remain less explored as a photocatalyst presumably due to their rather wide band gap that makes them active in the UV region alone, therefore restraining the practical use of Nb_2O_5 to ≤5%. Although Tsang and co-workers studied the shape-dependent acidity and photocatalytic activity of Nb_2O_5 nanocrystals, and found that Nb_2O_5 nanorods have higher activity than nanospheres,[25] the nanorods showed feeble absorption in the visible region, and the study was

Received: May 28, 2015
Accepted: August 4, 2015
Published: August 4, 2015

DOI: 10.1021/acsami.5b04667
ACS Appl. Mater. Interfaces 2015, 7, 17954−17962

Scheme 1

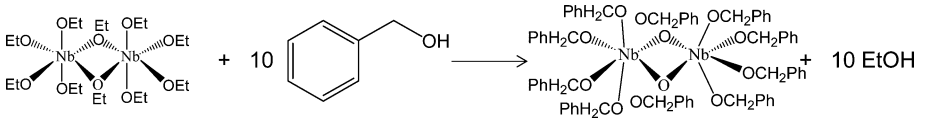

Scheme 2

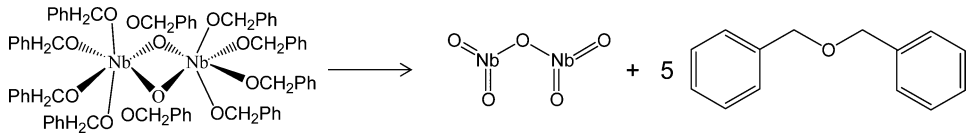

Scheme 3

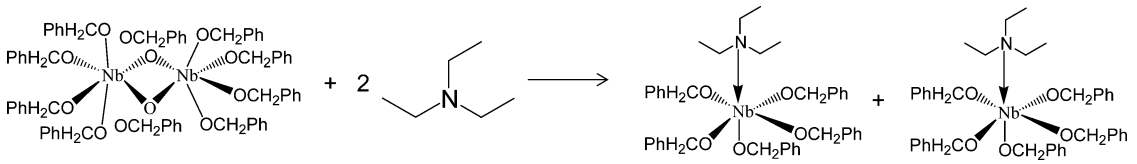

Scheme 4

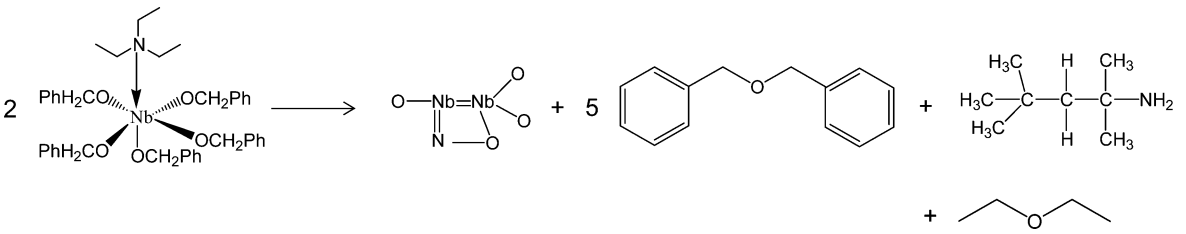

conducted under ultraviolet radiation. Thus, the development of 1-D Nb_2O_5 endowed with absorption in the visible region offers an attractive possibility. Among various approaches, nitrogen-doping has proved to be one of the most effective ways to attune photocatalysis to be more visible-light-driven.[26,27] In addition, N doping has significant impact on various physicochemical properties such as the oxidation stability, the conductivity and the electrochemical behavior, the adsorption capabilities, the basicity, and so forth, which affect the performance of the resulting catalysts. Although attempt has been made to extend the absorption threshold of mesoporous Nb_2O_5 from UV to visible by nitrogen doping, nanoparticles were made by heating Nb_2O_5 and urea at 400 °C, resulting in particles of irregular shapes.[28] While the shift of absorption threshold is crucial for efficient utilization of the solar spectrum, tailoring the particle shape is also important for photoactivity enhancement.

Here, we report for the first time, a facile low temperature solvothermal method for the preparation of a nanocomposite consisting of N-NbO*x* nanorods and reduced graphene oxide (RGO) in benzyl alcohol using triethyl amine (TEA), with the latter as a nitriding precursor as well as a capping agent. A plausible mechanism for the formation and isotropic growth of highly ordered N-NbO*x* nanorods along the (001) plane is proposed. Optical measurements indicate that the N-NbO*x*/RGO absorbs visible light, the extent of which shows strong dependence on the extent of nitrogen doping, which was precisely controlled by adjusting the molar ratio of Nb to N precursors during synthesis. Photoelectrochemical (PEC) study under visible (λ > 420 nm) and UV−visible light (λ = 300−600 nm) showed enhanced activity; a correlation between the photocurrent, amount of RGO, and nitrogen in Nb_2O_5 was also established.

2. EXPERIMENTAL SECTION

2.1. Materials Synthesis. Details of materials synthesis and PEC measurements are given in the Supporting Information. Briefly, N-NbO*x* was synthesized as follows: 0.03 mol of niobium ethoxide was added to 20 mL of benzyl alcohol solvent followed by the addition of desired molar ratio of triethyl amine (TEA). The resulting clear solution was transferred into a 45 mL Teflon reactor and heated at 250 °C for 3 days in a Parr autoclave. For the preparation of N-NbO*x*/RGO composite, graphene oxide was first dispersed in benzyl alcohol followed by niobium ethoxide and TEA addition.

2.2. Photoelectrocatalytic Activity. The PEC activity was studied in a three-electrode cell assembly connected to a potentiostat. A 0.1 M sodium sulfate solution was used as the electrolyte. Saturated calomel electrode and coiled platinum wires were used as the reference and counter electrode, respectively. The working electrode was prepared from a homogeneous suspension of Nafion and the catalyst in ethanol by sonication and deposited on an ITO substrate. A 300 W xenon lamp with a cutoff filter to obtain radiation of λ > 420 nm was used. The light intensity was measured to be 300 mW/cm^2.

3. RESULTS AND DISCUSSION

Nb(V) ions are known to form facile coordination complexes virtually with all types of donors: neutral as well as anionic. In some instances, this stems from the ability of Nb(V) compounds to act as Lewis acid. In the absence of any additional surfactants or reagents, the solvothermal reaction between niobium ethoxide and benzyl alcohol occurs in two steps. This involves ligand exchange reaction followed by ether elimination. Metal-ethoxy bridging renders the chemical formula of niobium ethoxide as

DOI: 10.1021/acsami.5b04667
ACS Appl. Mater. Interfaces 2015, 7, 17954−17962

$Nb_2(OC_2H_5)_{10}$, in bioctahedral arrangement as is the case with most of the alkoxides of such metals. The reaction of niobium ethoxide with benzyl alcohol to form niobium(V) oxide can be represented by the following schemes.[29,30] First, the ethoxy group is exchanged with the benzyl group, forming benzyl alkoxide via ethanol elimination (Scheme 1).

Such a ligand exchange is quite facile and can occur even at room temperature (often indicated by color change). Next, the alkoxy moiety undergoes condensation reaction to form the M−O−M bond, releasing the corresponding aromatic ether (Scheme 2):

TEA is endowed with a lone pair of electrons on the nitrogen atom; it also acts as a capping agent. It forms an adduct with niobium benzyl alkoxide by virtue of coordination bond between metal cation in the alkoxide and nitrogen in the TEA molecule by electron pair donation (Scheme 3):

The N-coordinated niobium complex is highly steric and labile, first undergoing rearrangement and then decomposing to yield a nitrogen-substituted niobium oxide (Scheme 4):

The FE-SEM images shown in Figure 1 highlight the transformational variation in the shape, morphology, and homogeneity of pure Nb_2O_5 (A) and N-NbO*x* (B). As evident, pure Nb_2O_5 grains have almost uniform, near-spherical shape with size in the range of 60 to 80 nm. In the presence of TEA, however, the morphology undergoes drastic change leading to the formation of a large number of nanorods. Thus, TEA appears to be bifunctional in the present case: (1) it served as a capping agent, restricting the lateral growth and facilitating the one-dimensional propagation of the Nb_2O_5 crystals, and (2) it acted as a nitrogen source, leading to the formation of N-NbO*x*. Change is morphology with respect to various Nb to TEA (or Nb to N) molar ratio is illustrated in Figure S1. Further in-depth characterization was carried out by TEM technique. In the case of N-NbO*x*, the diameter of the nanorods was in the range of ∼10−20 nm while the length ranged from submicron to a micron (Figure 1C). Figure 1D depicts a perfectly ordered assembly of large number of individual particles stacked together along the (001) direction. The electron diffraction and the HR-TEM microscopy images (Figure 1E and F) of N-NbO*x* show high degree of crystallinity. The interplanar distance for the [001] zone axis was computed to be 0.385 nm, in good agreement with 0.392 nm based on XRD data. The highly ordered morphological growth in N-NbO*x* suggests that while the early nucleation of nanoparticles is synchronous with ethanol elimination and condensation steps, subsequent orientation and texturing is greatly influenced by TEA and the organic species formed in situ. This, together with the perfectly uniform stacking (Figure 1D), reveals pseudosingle crystal nature of the nanoplatelets, thus supporting the notion of systematic addition of identical platelets in succession, subsequent to the fusion of several small crystallite on the host platelet. Thus, a given platelet acts like a substrate by itself, allowing the subsequent crystals to nucleate and grow in the preferred direction of the host structure. The absence of a significant level of lattice mismatch (or nonalignment) either among the primary building blocks or subsequent additive layers, that could otherwise result in major stacking faults and other defects (such as dislocation) leading to not-so-perfect modular structure is noteworthy. Thus, instead of individual particles, a perfectly homogeneous supercrystalline nanostructure results. This indicates that the alcohol in the reaction mixture in hyperstoichiometric ratio aids the ethanol elimination; the mesomerism in benzyl alcohol (akin to resonance effect in inorganic compounds) also plays a role in causing inductive effect. The nonuniform electron charge distribution at the terminal groups in the molecule assists stabilization of transition states through which ethanol is eliminated. The presence of $\pi-\pi$ bonding and significant steric effect in aromatic compounds is also operative in holding the Nb-complex together, from which Nb_2O_5 is eventually formed. Interestingly, in the presence of TEA, formation of N-NbO*x* nanorods was observed, which could be attributed to the capping effect of the amine. In addition to suppressing the abnormal growth of the Nb_2O_5 particles, the amine molecules, due to significant steric hindrance, also tend to align themselves in a linear fashion with respect to the metal and the ligand. This would terminate the lateral growth of the particles, resulting predominantly in the formation of 1-D structure, as illustrated in Figure 2. Finally, the elimination of byproducts leads to the formation of highly crystalline nanorods of pure N-NbO*x*.

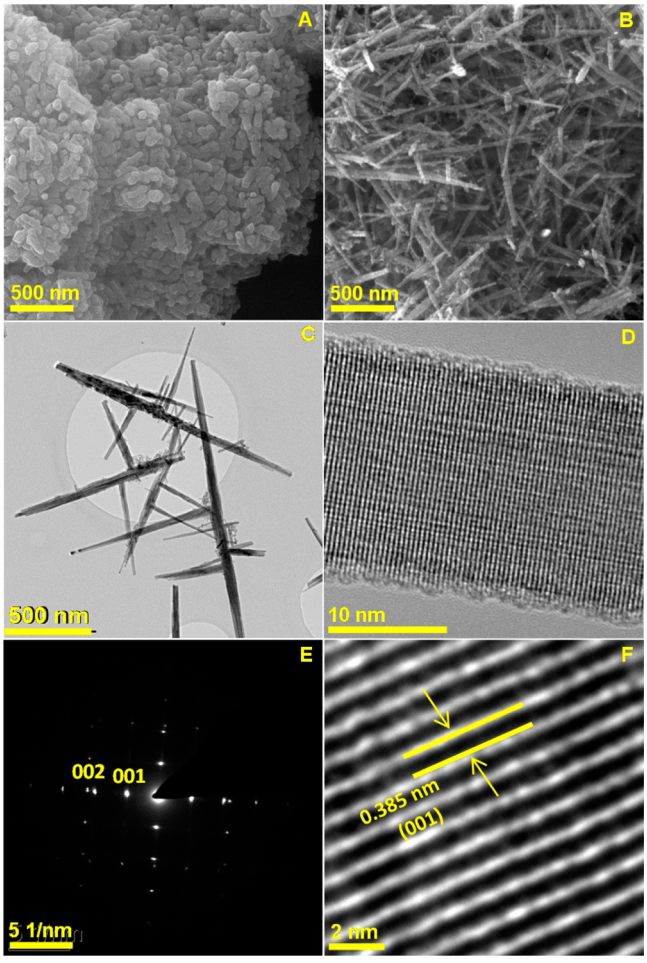

Figure 1. FE-SEM images of (A) Nb_2O_5 nanoparticles and (B) N-NbO*x* nanorods, (C,D) TEM images of N-NbO*x*, (E) SAED patterns, and (F) HR-TEM of N-NbO*x* nanorods.

The XRD patterns of pure and doped Nb_2O_5 are shown in Figure 3 which conform to that for orthorhombic Nb_2O_5 (T-phase; JCPDS 30-0873). The diffraction peaks at 22.41°, 28.48°, 36.65°, and 45.99° (2θ) could be indexed as ⟨001⟩, ⟨100⟩, ⟨101⟩, and ⟨002⟩, respectively. It is worth pointing out that, despite the use of rather mild and moderate synthesis parameters, the XRD signatures are indicative of compound formation in highly crystalline state. Moreover, the ⟨001⟩ reflection is the strongest, suggesting that the preferred growth was along the ⟨001⟩ plane.

DOI: 10.1021/acsami.5b04667
ACS Appl. Mater. Interfaces 2015, 7, 17954−17962

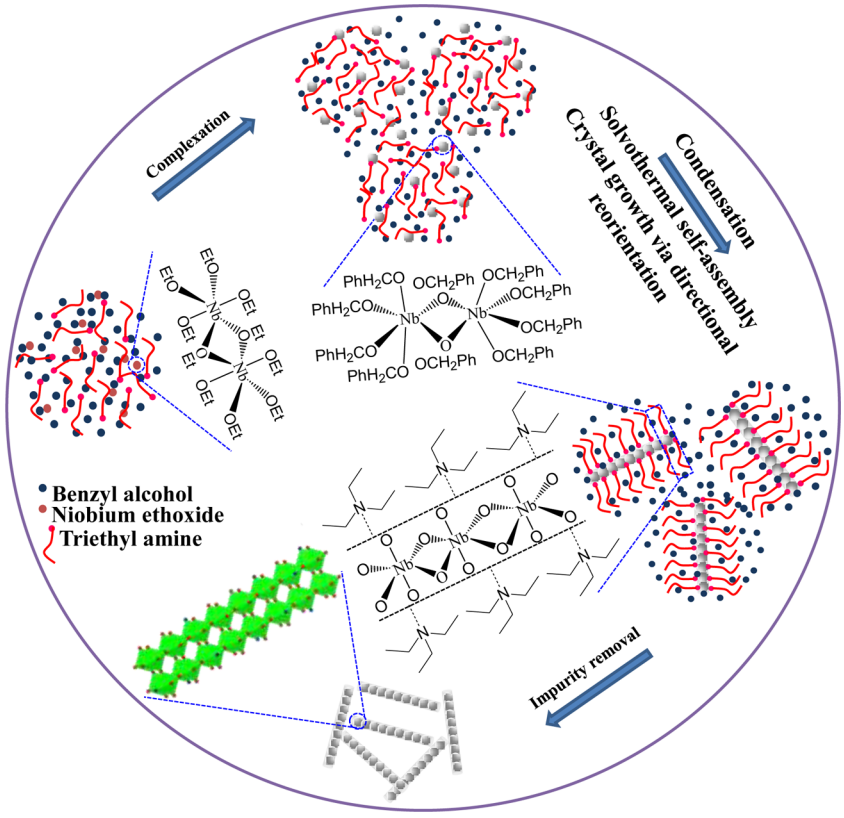

Figure 2. Illustrative sequence of the formation, crystallization, and self-assembly scheme in N-NbO*x* nanorods.

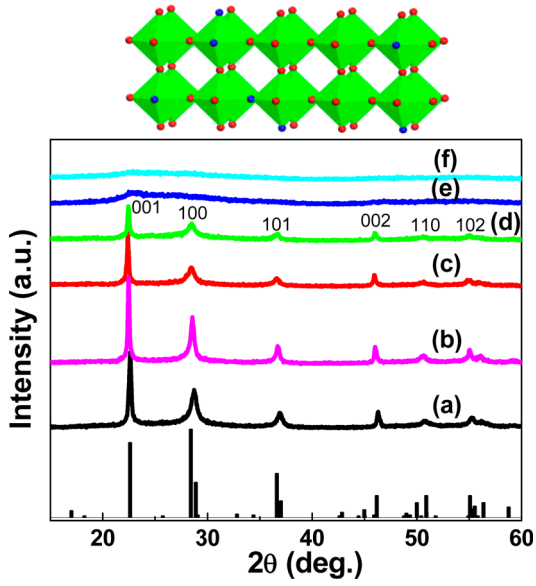

Figure 3. XRD patterns of Nb_2O_5 by nonaqueous route with Nb to N molar ratio of (b) 1:1, (c) 1:2, (d) 1:3, (e) 1:4, and (f) 1:5. Spectrum (a) is for the undoped Nb_2O_5. The standard pattern for orthorhombic (T-phase) Nb_2O_5 is shown at the bottom whose skeletal motif of the T-phase Nb_2O_5 with possible arrangement of oxygen (red), nitrogen (blue), and niobium (within the polyhedron) is also included.

The calculated lattice parameters were a = 6.175, b = 29.175, and c = 3.930 Å, and the crystallite size estimated from Scherrer equation was 40 nm.[31] In the presence of TEA, noticeable changes in the morphology and crystallinity were observed. For a given amount of benzyl alcohol, the crystallinity decreases progressively with increasing mol/mol ratio of TEA/$Nb_2(OEt)_{10}$. Beyond an optimal concentration of TEA (Nb/N > 1:4 mol/mol), the crystallization kinetics become sluggish and even reversed, resulting in the formation of N-NbO*x* as an amorphous phase, whose microstructural features (Figure S1) indicated the coexistence of nanorods and nanoparticles.

Nitrogen incorporation in the Nb_2O_5 lattice was investigated by XPS of pure as well as the N-NbO_x samples. Atom % of nitrogen with respect to Nb to N molar ratio was measured to be 0.0, 0.65, 1.62, 2.96, 3.12, and 3.15 for 1:0, 1:1, 1:2, 1:3, 1:4, and 1:5, respectively. Respective elemental spectra for pure Nb_2O_5 sample are shown in Figure 4, while those in the case of a representative doped sample (Nb/N ratio 1:3) are shown in Figure 5. XPS analysis confirmed the nitrogen insertion in the Nb_2O_5 lattice. The binding energy peaks at 207.2 and 209.8 eV belong to the Nb $3d_{5/2}$ and Nb $3d_{3/2}$ spectral line, respectively; these are in good agreement with those reported in the literature for Nb_2O_5.[32] The peaks at 530.3 and 531 eV represent O coordinated with Nb and, with either H (in OH) or N, respectively. The peaks at 284.6 and 286 eV for C 1s belong to the contaminant carbon (C−C) and C−O or C−OH binding in benzyl alcohol.[33] In the case of nitrogen, the somewhat diffuse peak at 395.1 eV could be ascribed to the substitutional N bonding (or β-N) in N-NbO_x; the peak ∼396 eV has been identified as due to the substitution of β-N for O in metal oxide lattice.[34] The second rather strong peak at 401.6 eV is likely due to anionic N (or γ-N) in the O−Nb−N ring.[35] This is supported by the fact that the amount of anionic N increased with increase in amine level in the mixture, suggesting γ-N substitution in the Nb_2O_5 lattice. Thus, it is reasonable to infer that in the presence of triethyl amine, N is effectively incorporated into the matrix of Nb_2O_5 (Schemes 3 and 4) via β-N and/or γ-N substitution. It is

DOI: 10.1021/acsami.5b04667
ACS Appl. Mater. Interfaces 2015, 7, 17954−17962

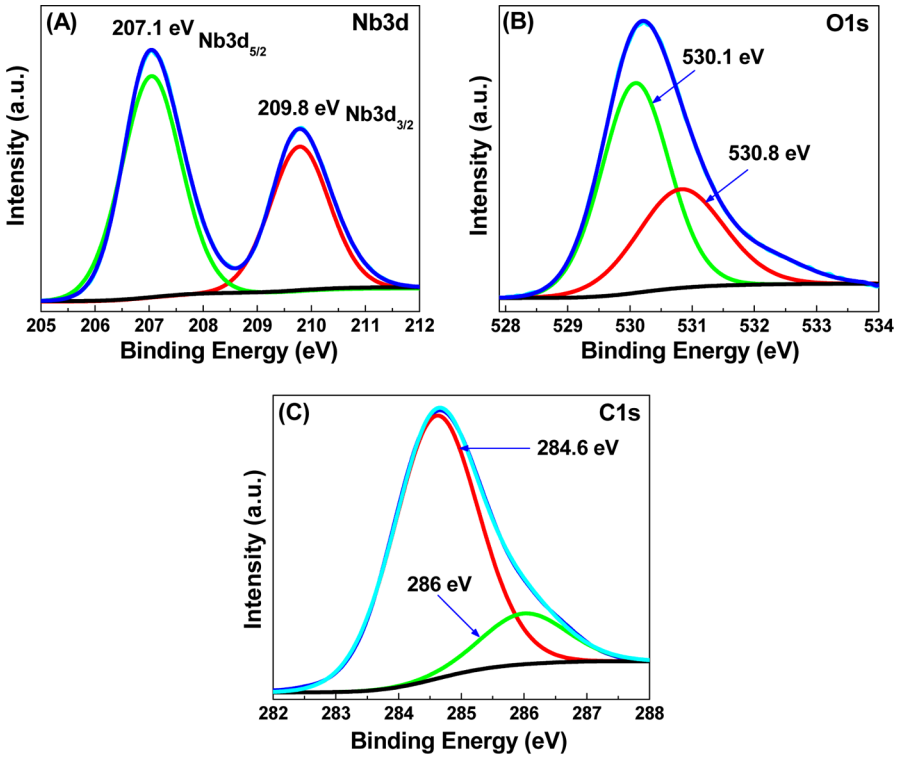

Figure 4. XPS signatures of pure Nb_2O_5: (A) Nb 3d, (B) O 1s, and (C) C 1s.

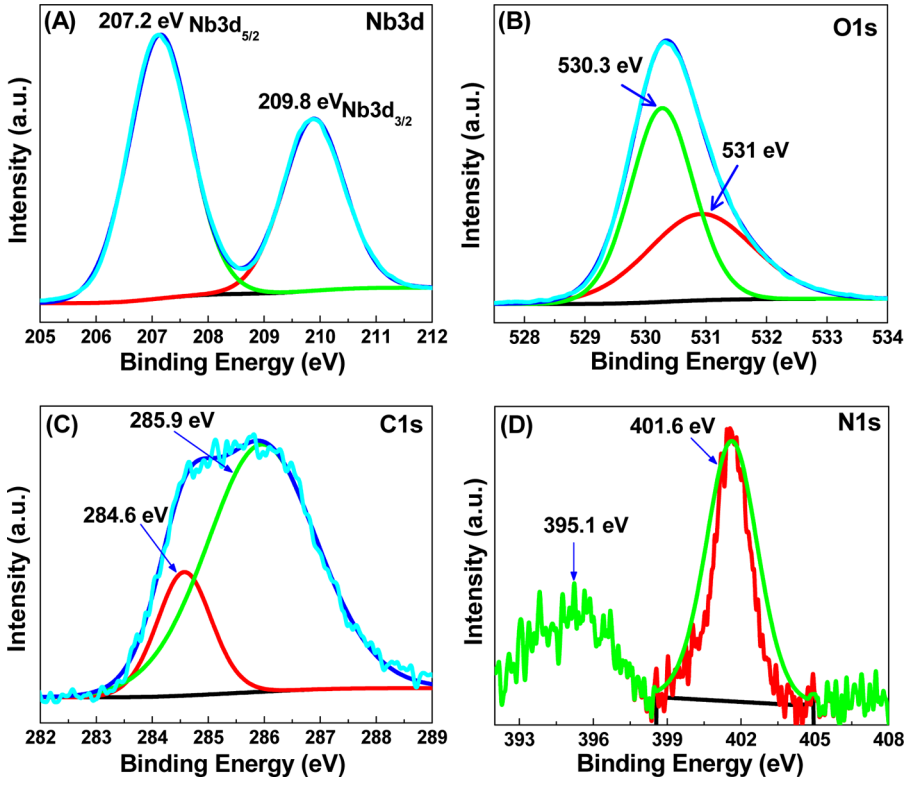

Figure 5. Binding energy spectra of N-NbO_x nanorods with Nb/N molar ratio 1:3: (A) Nb 3d, (B) O 1s, (C) C 1s, and (D) N 1s.

worthpointing that no nitrogen peaks were present in the XPS of pure Nb_2O_5 (Figure 4).

The results of DRS examination conducted on pure and N-NbO*x* samples show systematic variation in the material properties in term of monotonic variation in their optical properties as a result of doping. As shown in Figure S3, clearly there are spectral shifts toward higher wavelength concomitant with the increase in the dopant level. This is elegantly manifested in the systematic decrease in the indirect band gap energy with increase in the dopant level. A correlation between the

DOI: 10.1021/acsami.5b04667
ACS Appl. Mater. Interfaces 2015, 7, 17954−17962

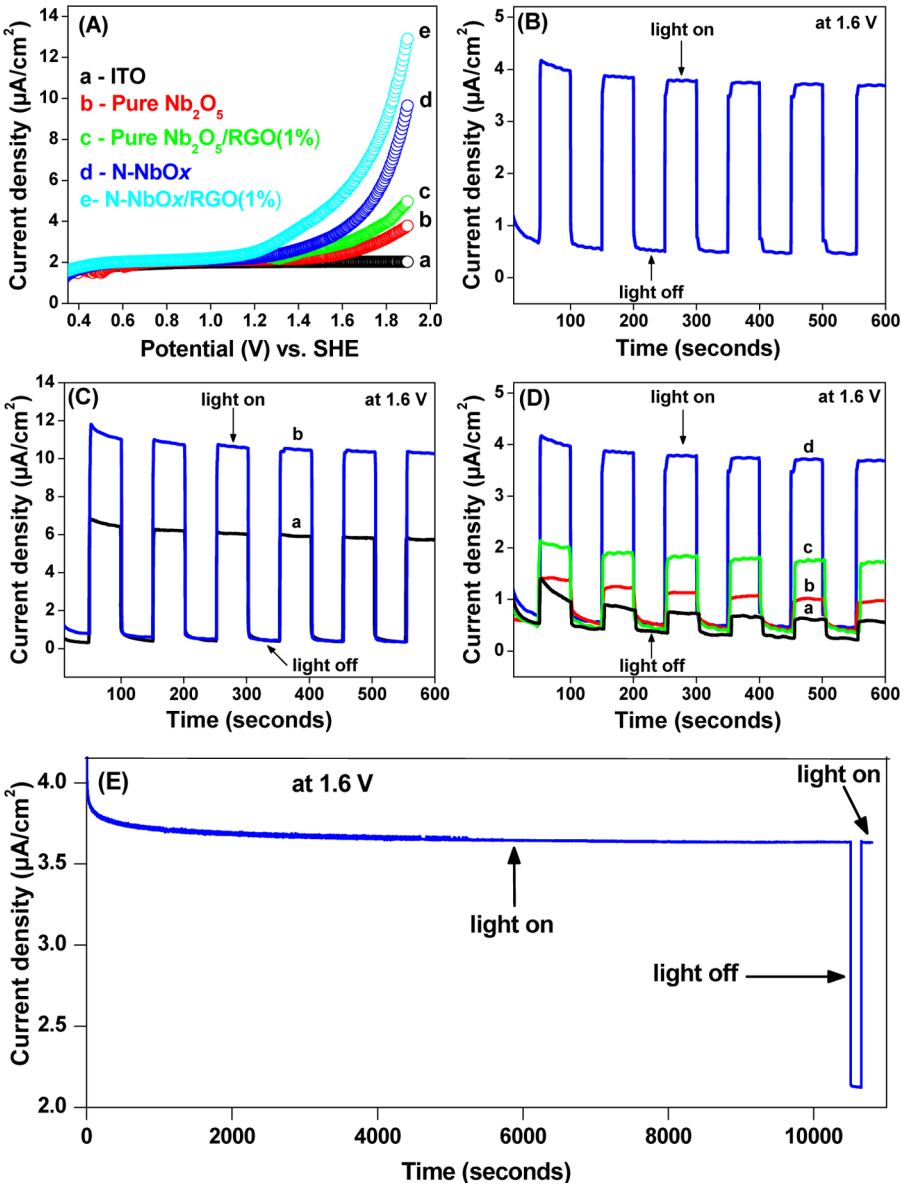

Figure 6. (A) Comparative potentiodynamic (I–V) response of various formulations; (B) reproducible variation of photocurrent under intermittent visible light illumination of the N-NbOx nanorods; (C) comparative photocurrent profiles of (a) pristine Nb_2O_5 nanoparticles and (b) N-NbOx nanorods under intermittent UV–visible light illumination; (D) comparative photocurrent profiles of (a) pristine Nb_2O_5 nanoparticles, (b) pristine Nb_2O_5 nanorods, (c) N-doped Nb_2O_5 nanoparticles, and (d) N-NbOx nanorods under intermittent visible light illumination; (E) evidence of stability and reproducibility of the photocurrent in the case of N-NbOx nanorods. The molar ratio of Nb/N in the N-NbOx nanorods was 1:3.

theoretical molar ratio of the niobium precursor and triethyl amine and, the calculated band gap is shown in Figure S4. The atom % of nitrogen in each of the doped samples was determined by XPS and is also presented in Figure S4. Moreover, the band positions of pristine and N-doped Nb_2O_5 samples were calculated by following the below empirical formulas[36] and the values are listed in Table S1.

$$E_{CB} = X - E_c - 1/2E_g$$

$$E_{VB} = E_{CB} + E_g$$

where E_{CB} = the conduction band, X = the absolute electronegativity of the atoms, expressed as the geometric mean of the absolute electronegativity of the constituent atoms, which is defined as the arithmetic mean of the atomic electron affinity and the first ionization energy, E_c = the energy of free electrons of the hydrogen scale (4.5 eV), E_g = the band gap, and E_{VB} = the valence band.

The anodic polarization (photoelectrocurrent density vs potential) profiles for pure Nb_2O_5, Nb_2O_5/RGO, N-NbOx, and N-NbOx/RGO nanocomposite, in the presence of visible light, are shown in Figure 6A. As can be seen, during the voltage sweep (5 mV/s), the current density was approximately 4 μA cm^{-2} at 1.9 V_{SHE} for pure Nb_2O_5 (Figure 6A), which was slightly increased when composited with RGO. However, photocurrent was increased to ~10 μA cm^{-2} in the case of N-NbOx with Nb/N molar ratio of 1:3. Such response amelioration could be attributed to the combined effect of morphology and enhanced light absorption as a result of shift in absorption threshold to lower energy end caused by nitrogen doping. This notion is strengthened by the DRS studies (Figure S3) in terms of systematic decrease of the energy band gap. Further improve-

DOI: 10.1021/acsami.5b04667
ACS Appl. Mater. Interfaces 2015, 7, 17954–17962

ment (~1.3 fold) in the photoelectrocurrent densities during the anodic polarization experiments was achieved by making nanocomposites of the N-NbO*x* with reduced graphene oxide, where RGO acted as a solid-state electron mediator (Figure 6A). The N-NbO*x*/RGO nanocomposite achieved approximately 3.4 fold improvement in the respective photoelectrocurrent density values, compared to those for the undoped and uncomposited pure Nb_2O_5. Since, both nitrogen and RGO seem to be responsible in modifying the photoelectrochemical behavior of Nb_2O_5, their respective effects were quantified in terms of photoelectrocurrent density, and the results are shown in Figures S5 and S6, respectively. The RGO in the present work is derived from graphene oxide (GO) which we speculate was partially reduced in situ to RGO in the presence of benzyl alcohol which has strong reducing attributes. In order to substantiate this speculation about the role of benzyl alcohol in the chemical reduction of GO into RGO, GO alone was thoroughly dispersed in benzyl alcohol via ultrasonication followed by heating in a Teflon autoclave at 250 °C for 3 days (mimicking the experimental conditions of Nb_2O_5 synthesis). The Raman spectrum of the product shown in Figure 7 indicates a small

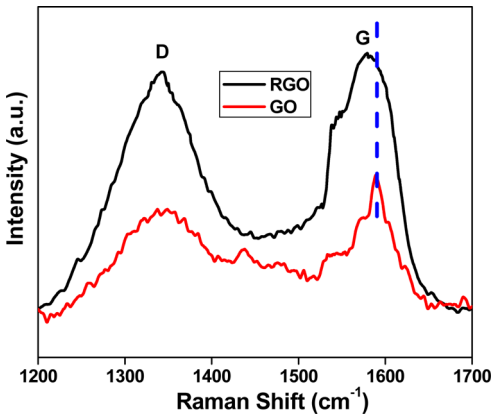

Figure 7. Raman signatures of graphene oxide (GO) and reduced graphene oxide (RGO).

blue-shift of the G-band, which signals partial reduction of graphene oxide. Moreover, the (D-band/G-band) intensity ratio was also slightly higher than that of pristine GO, indicating a decrease in the sp^2 hybridization due to the reduction of exfoliated GO.[28,37] In-situ formation of RGO layers in the nanocomposite is also substantiated by the microscopic images (Figure S7). Since the photoelectrodes may show a certain degree of current drift over a time scales of 5−10 min and hence creates ambiguity between photocurrents under illumination and currents under dark. Figure 6B shows the variation of photocurrent (under illumination and dark conditions) of N-NbO*x* (Nb/N = 1:3) by switching the light on and off for ~10 min at a constant applied load of 1.6 V. The photocurrent generated instantaneously upon illumination and reached a steady state while very low current was observed under dark, even at high applied potential (1.6 V). The PEC of the pure as well as N-doped Nb_2O_5 (with the above-mentioned Nb:N molar ratio) was also examined under UV−visible radiation (Figure 6C). Evidently, the photoelectrocurrent was significantly enhanced in both the cases as a result of the presence of high energy photons generated by UV light. Furthermore, the current in the case of N-NbO*x* nanorods was ~1.5 times greater than that in the case of pure Nb_2O_5 nanoparticles. The data summarized in Figure 6D, compares the photoelectrochemical attributes of pure and doped Nb_2O_5 of different morphologies (nanoparticles vs nanorods) under visible light. These were synthesized by different methods as described in literature[25,28] (see the Supporting Information). As can be readily seen, pristine Nb_2O_5 nanorods showed slightly higher photocurrent than the nanoparticles. A similar trend was observed in the case of N-doped samples; the N-NbO*x* nanorods showed relatively higher photocurrent as compared to that by pure Nb_2O_5 nanorods or N-doped Nb_2O_5 nanoparticles. This could be attributed to the synergy brought by effective nitrogen incorporation and the resulting 1-D morphology in the case of N-NbO*x*. Figure 6E depicts the stability of N-NbO*x* (change in photoelectrocurrent with respect to time) under applied experimental conditions. Initially, the photocurrent was slightly declined and then remained constant up to 3 h. As evident, the photocurrent dropped significantly under dark and again generated instantaneously upon illumination and reached a steady state. This clearly indicated the good stability of N-NbO*x* under visible light irradiation and constant applied potential.

In the light of the foregoing discussion, the mechanistic aspects of the improved photoelectrochemical performance of the N-NbO_x/RGO nanocomposite are summarized in Figure 8. Briefly,

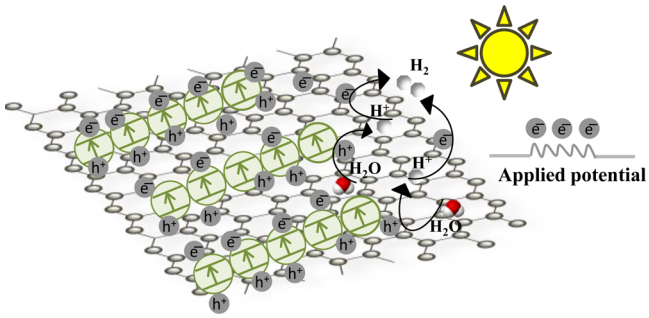

Figure 8. Plausible mechanism for water splitting in the presence of N-NbO*x*/RGO under photoelectrochemical stimuli.

when energized by light of energy that is either equal to or greater than the band gap energy of N-NbO*x* (>420 nm in this case), electrons are promoted from the valence band (e^-_{vb}) to the conduction band (e^-_{cb}), leaving behind an electron hole in the valence band (h^+_{vb}). If the charge separation is maintained, the electron−hole pair would migrate to the catalyst surface where they participate in redox reactions with sorbed species. The h^+_{vb} radical would react with surface-bound H_2O or OH^- to produce hydroxyl radical ($OH^\bullet$), which upon oxidation produce O_2; the e^-_{cb} is scavenged by H^+ ions to produce $H^\bullet$ and subsequently H_2. One of the overriding limitations and energy-wasting step involved in photocatalytic processes is the recombination of the e^-_{cb} and h^+_{vb} pair. Presence of RGO in the nanocomposite is likely to create a heterojunction that disallows recombination, thus facilitating the preferential transfer of e^-_{cb} from interfacial region from photocatalyst to the RGO surface. This mitigates the undesired recombination, thereby improving the photoelectrochemical performance.

4. CONCLUSIONS

In summary, a facile solvothermal route was developed for the synthesis of a highly homogeneous and uniform nanocomposite of reduced graphene oxide and low-dimensional N-doped Nb_2O_5 with preferred crystallization in the ⟨001⟩ plane in the presence of triethyl amine; TEA performs dual functions, both as a

DOI: 10.1021/acsami.5b04667
ACS Appl. Mater. Interfaces 2015, 7, 17954−17962

nitrogen source and, a capping agent. The nanocomposite was shown to be an efficient photoelectrochemical agent for water splitting under both visible as well as UV−visible light. A mechanism for the formation and directional growth of N-doped Nb_2O_5 and its enhanced photoelectrochemical activity has been proposed. The unique acicular morphology of N-doped Nb_2O_5 compound together with the benign effect of RGO on the photoelectrochemical water splitting process suggests that such nanocomposites are likely to find numerous applications in other applied areas, such as lithium ion batteries, gas sensing, electrochromics, microelectronics, and others.

■ ASSOCIATED CONTENT

Supporting Information

The Supporting Information is available free of charge on the ACS Publications website at DOI: 10.1021/acsami.5b04667.

Synthesis of pure Nb_2O_5, N-NbO*x*, graphene oxide (GO), N-NbO*x*/reduced graphene oxide (RGO) nanocomposites, N-doped Nb_2O_5 nanoparticles, Nb_2O_5 nanorods, photoelectrochemical characterization, change in morphology (SEM images) with respect to Nb/TEA molar ratio, HR-TEM images, diffuse reflectance spectroscopy (DSR), systematic band gap variation with atom % of nitrogen, band edge positions, effect of Nb to N molar ratio and RGO content on photocurrents, FESEM and TEM images showing the presence of transparent RGO layers in the composite, and SEM, XRD, and DRS of N-doped Nb_2O_5 nanoparticles and Nb_2O_5 nanorods (PDF)

■ AUTHOR INFORMATION

Corresponding Author

*E-mail: qamar@kfupm.edu.sa (M.Q.).

Author Contributions

The manuscript was written through the contributions of all authors. All authors have given approval to the final version of the manuscript.

Notes

The authors declare no competing financial interest.

■ ACKNOWLEDGMENTS

This project was funded by National Plan for Science, Technology and Innovation (MAARIFAH), King Abdulaziz City for Science and Technology (KACST) through the Science & Technology Unit at King Fahd University of Petroleum & Minerals (KFUPM), Kingdom of Saudi Arabia, Award Number (10-NAN1387-04).

■ REFERENCES

(1) Qamar, M.; Khan, A. Mesoporous Hierarchical Bismuth Tungstate as a Highly Efficient Visible-Light-Driven Photocatalyst. *RSC Adv.* **2014**, *4*, 9542−9550.

(2) Martin, D. J.; Qiu, K.; Shevlin, S. A.; Handoko, A. D.; Chen, X.; Guo, Z.; Tang, J. Highly Efficient Photocatalytic H_2 Evolution from Water Using Visible Light and Structure-Controlled Graphitic Carbon Nitride. *Angew. Chem., Int. Ed.* **2014**, *53*, 9240−9245.

(3) Shannon, M. A.; Bohn, P. W.; Elimelech, M.; Georgiadis, J. G.; Mariñas, B. J.; Mayes, A. M. Science and Technology for Water Purification in the Coming Decades. *Nature* **2008**, *452*, 301−310.

(4) Chong, M. N.; Jin, B.; Chow, C. W.; Saint, C. Recent Developments in Photocatalytic Water Treatment Technology: A Review. *Water Res.* **2010**, *44*, 2997−3027.

(5) Xu, Q.; Yu, J.; Zhang, J.; Zhang, J.; Liu, G. Cubic Anatase TiO_2 Nanocrystals with Enhanced Photocatalytic CO_2 Reduction Activity. *Chem. Commun.* **2015**, *51*, 7950−7953.

(6) Yin, G.; Nishikawa, M.; Nosaka, Y.; Srinivasan, N.; Atarashi, D.; Sakai, E.; Miyauchi, M. Photocatalytic Carbon Dioxide Reduction by Copper Oxide Nanocluster-Grafted Niobate Nanosheets. *ACS Nano* **2015**, *9*, 2111−2119.

(7) Wang, J.; Pan, S.; Chen, M.; Dixon, D. A. Gold Nanorod-Enhanced Light Absorption and Photoelectrochemical Performance of α-Fe_2O_3 Thin-Film Electrode for Solar Water Splitting. *J. Phys. Chem. C* **2013**, *117*, 22060−22068.

(8) Edman Jonsson, G.; Fredriksson, J. H.; Sellappan, R.; Chakarov, D. Nanostructures for Enhanced Light Absorption in Solar Energy Devices. *Int. J. Photoenergy* **2011**, *2011*, 1−11.

(9) Tao, J.; Batzill, M. Role of Surface Structure on the Charge Trapping in TiO_2 Photocatalysts. *J. Phys. Chem. Lett.* **2010**, *1*, 3200−3206.

(10) Kumar, S. G.; Rao, K. S. R. K. Zinc Oxide Based Photocatalysis: Tailoring Surface-Bulk Structure and Related Interfacial Charge Carrier Dynamics for Better Environmental Applications. *RSC Adv.* **2015**, *5*, 3306−3351.

(11) Simon, T.; Bouchonville, N.; Berr, M. J.; Vaneski, A.; Adrović, A.; Volbers, D.; Wyrwich, R.; Döblinger, M.; Susha, A. S.; Rogach, A. L.; Jäckel, F.; Stolarczyk, J. K.; Feldmann, J. Redox Shuttle Mechanism Enhances Photocatalytic H_2 Generation on Ni-Decorated CdS Nanorods. *Nat. Mater.* **2014**, *13*, 1013−1018.

(12) Xi, G.; Ye, J. Synthesis of Bismuth Vanadate Nanoplates with Exposed {001} Facets and Enhanced Visible Light Photocatalytic Properties. *Chem. Commun.* **2010**, *46*, 1893−1895.

(13) Yang, H. G.; Liu, G.; Qiao, S. Z.; Sun, C. H.; Jin, Y. G.; Smith, S. C.; Zou, J.; Cheng, H. M.; Lu, G. Q. Solvothermal Synthesis and Photoreactivity of Anatase TiO_2 Nanosheets with Dominant {001} Facets. *J. Am. Chem. Soc.* **2009**, *131*, 4078−4083.

(14) Yang, H. G.; Sun, C. H.; Qiao, S. Z.; Zou, J.; Liu, G.; Smith, S. C.; Cheng, H. M.; Lu, G. Q. Anatase TiO_2 Single Crystals with a Large Percentage of Reactive Facets. *Nature* **2008**, *453*, 638−641.

(15) Nguyen, T.-D. From Formation Mechanisms to Synthetic Methods Toward Shape-Controlled Oxide Nanoparticles. *Nanoscale* **2013**, *5*, 9455−9482.

(16) Gordon, T. R.; Cargnello, M.; Paik, T.; Mangolini, F.; Weber, R. T.; Fornasiero, P.; Murray, C. B. Nonaqueous Synthesis of TiO_2 Nanocrystals Using TiF_4 to Engineer Morphology, Oxygen Vacancy Concentration, and Photocatalytic Activity. *J. Am. Chem. Soc.* **2012**, *134*, 6751−6761.

(17) Wang, X.; Jiang, Z.; Zheng, B.; Xie, Z.; Zheng, L. Synthesis and Shape-Dependent Catalytic Properties of CeO_2 Nanocubes and Truncated Octahedra. *CrystEngComm* **2012**, *14*, 7579−7582.

(18) Augustyn, V.; Come, J.; Lowe, M. A.; Kim, J. W.; Taberna, P.-L.; Tolbert, S. H.; Abruña, H. D.; Simon, P.; Dunn, B. High-Rate Electrochemical Energy Storage Through Li^+ Intercalation Pseudocapacitance. *Nat. Mater.* **2013**, *12*, 518−522.

(19) Rani, R. A.; Zoolfakar, A. S.; O'Mullane, A. P.; Austin, M. W.; Kalantar-Zadeh, K. Thin Films and Nanostructures of Niobium Pentoxide: Fundamental Properties, Synthesis Methods and Applications. *J. Mater. Chem. A* **2014**, *2*, 15683−15703.

(20) Zhao, Y.; Zhou, X.; Ye, L.; Tsang, S. C. E. Nanostructured Nb_2O_5 Catalysts. *Nano Rev.* **2012**, *3*, 17631−17641.

(21) Fiz, R.; Hernandez-Ramirez, F.; Fischer, T.; Lopez-Conesa, L.; Estrade, S.; Peiro, F.; Mathur, S. Synthesis, Characterization, and Humidity Detection Properties of Nb_2O_5 Nanorods and SnO_2/Nb_2O_5 Heterostructures. *J. Phys. Chem. C* **2013**, *117*, 10086−10094.

(22) Li, B.; Gu, M.; Nie, Z.; Wei, X.; Wang, C.; Sprenkle, V.; Wang, W. Nanorod Niobium Oxide as Powerful Catalysts for an All Vanadium Redox Flow Battery. *Nano Lett.* **2014**, *14*, 158−165.

(23) Zhang, H.; Wang, Y.; Yang, D.; Li, Y.; Liu, H.; Liu, P.; Wood, B. J.; Zhao, H. Directly Hydrothermal Growth of Single Crystal $Nb_3O_7(OH)$ Nanorod Film for High Performance Dye-Sensitized Solar Cells. *Adv. Mater.* **2012**, *24*, 1598−1603.

DOI: 10.1021/acsami.5b04667
ACS Appl. Mater. Interfaces 2015, 7, 17954−17962

(24) Singh, C.; Pandey, M. K.; Biradar, A. M.; Srivastava, A. K.; Sumana, G. A Bienzyme-Immobilized Highly Efficient Niobium Oxide Nanorod Platform for Biomedical Application. *RSC Adv.* **2014**, *4*, 15458−15465.
(25) Zhao, Y.; Eley, C.; Hu, J.; Foord, J. S.; Ye, L.; He, H.; Tsang, S. C. E. Shape-Dependent Acidity and Photocatalytic Activity of Nb_2O_5 Nanocrystals with an Active TT (001) Surface. *Angew. Chem., Int. Ed.* **2012**, *51*, 3846−3849.
(26) Asahi, R.; Morikawa, M. T.; Ohwaki, T.; Aoki, K.; Taga, Y. Visible-Light Photocatalysis in Nitrogen-Doped Titanium Oxides. *Science* **2001**, *293*, 269−271.
(27) Zhang, J.; Wu, Y.; Xing, M.; Leghari, S. A. K.; Sajjad, S. Development of Modified N Doped TiO_2 Photocatalyst with Metals, Nonmetals and Metal Oxides. *Energy Environ. Sci.* **2010**, *3*, 715−726.
(28) Huang, H.; Wang, C.; Huang, J.; Wang, X.; Du, Y.; Yang, P. Structure Inherited Synthesis of N-Doped Highly Ordered Mesoporous Nb_2O_5 as Robust Catalysts for Improved Visible Light Photoactivity. *Nanoscale* **2014**, *6*, 7274−7280.
(29) Pinna, N.; Niederberger, M. Surfactant-Free Nonaqueous Synthesis of Metal Oxide Nanostructures. *Angew. Chem., Int. Ed.* **2008**, *47*, 5292−5304.
(30) Garnweitner, G. Nonaqueous Syntheses of Metal Oxide and Metal Nitride Nanoparticles. Dissertation, Universität Potsdam, 2005.
(31) Patterson, A. The Scherrer Formula for X-Ray Particle Size Determination. *Phys. Rev.* **1939**, *56*, 978−982.
(32) Furukawa, S.; Shishido, T.; Teramura, K.; Tanaka, T. Photocatalytic Oxidation of Alcohols over TiO_2 Covered with Nb_2O_5. *ACS Catal.* **2012**, *2*, 175−179.
(33) Jia, H. M.; Xiao, W. J.; Zhang, L. Z.; Zheng, Z.; Zhang, H. L.; Deng, F. In Situ l-Hydroxyproline Functionalization and Enhanced Photocatalytic Activity of TiO_2 Nanorods. *J. Phys. Chem. C* **2008**, *112*, 11379−11384.
(34) Wang, R. W.; Zhu, Y. F.; Qiu, Y. F.; Leung, C. F.; He, J.; Liu, G. J.; Lau, T. C. Synthesis of Nitrogen-Doped $KNbO_3$ Nanocubes with High Photocatalytic Activity for Water Splitting and Degradation of Organic Pollutants Under Visible Light. *Chem. Eng. J.* **2013**, *226*, 123−130.
(35) Sathish, M.; Viswanathan, B.; Viswanath, R. P.; Gopinath, C. S. Synthesis, Characterization, Electronic Structure, and Photocatalytic Activity of Nitrogen-Doped TiO_2 Nanocatalyst. *Chem. Mater.* **2005**, *17*, 6349−6353.
(36) Dong, H.; Chen, G.; Sun, J.; Feng, Y.; Li, C.; Lv, C. Stability, Durability and Regeneration Ability of a Novel Ag-Based Photocatalyst $Ag_2Nb_4O_{11}$. *Chem. Commun.* **2014**, *50*, 6596−6599.
(37) Lv, X. J.; Fu, W. F.; Chang, H. X.; Zhang, H.; Cheng, J. S.; Zhang, G. J.; Song, Y.; Hu, C. Y.; Li, J. H. Hydrogen Evolution from Water Using Semiconductor Nanoparticle/Graphene Composite Photocatalysts Without Noble Metals. *J. Mater. Chem.* **2012**, *22*, 1539−1546.

DOI: 10.1021/acsami.5b04667
ACS Appl. Mater. Interfaces 2015, 7, 17954−17962